

# Geologically constrained 2D and 3D airborne EM inversion through cross-gradient regularization and multi-grid efficiency

**C. Scholl**  
CGG, Berlin  
Carsten.Scholl@CGG.com

**J. Neumann**  
CGG, Berlin  
Jan.Neumann@CGG.com

**M. D. Watts**  
CGG, Milan  
Don.Watts@CGG.com

**S. Hallinan**  
CGG, Milan  
Stephen.Hallinan@CGG.com

**S. Mulè\***  
CGG, Perth  
Shane.Mule@CGG.com

\*presenting author

## SUMMARY

With a goal of increasing the geological reliability of single and joint domain inversion, including those set in rugged terrain, we present an expanded scope for cross-gradient regularized inversion. The basic application covers the usual structural similarity objective – comparing the gradient fields of distinct property volumes derived from different geophysical domains – but a particular advantage comes when including gradients derived *a priori*, from geology or any ancillary property set, providing reference gradient control during single or joint inversions.

In the first example, straightforward cross-gradient joint inversion of synthetic datasets of airborne EM (AEM) and airborne gravity-gradiometry (AGG) improves both the lateral and vertical definition of closely adjacent but distinct bodies.

Two further AEM examples include surface and subsurface geology in the cross-gradient inversion; a) complex foothills setting, and b) buried massive sulphide. Both outputs demonstrate a marked improvement in interpretability over the standard smooth model approach.

**Key words:** Cross-Gradient, Geosteered, Inversion, Electromagnetics, Gradiometry

## INTRODUCTION

The standard approach for the quantitative interpretation of airborne electromagnetic data is still based on 1D imaging or inversion algorithms (e.g. Vallée and Smith, 2007), and while these are economic to run, they tend to produce spurious features in the presence of local anomalies, steeply dipping or complex geology, and in rugged topography. In order to overcome these limitations, multidimensional inverse algorithms (e.g. Cox *et al.*, 2012) can be employed to invert a model that is typically discretised into a vast number of cells. The downside – apart from the greatly increased computational cost – is that to achieve stability the algorithms require some form of model regularization, such as a smoothing operator, and therefore output models that may fit the data well enough but appeal less to the geologist.

In this paper we show examples of joint inversion of AEM and AGG, with an implementation similar to Gallardo and Meju (2003)'s cross-gradient application for DC resistivity and seismic travel time, and advance this process with examples of geosteered joint inversion incorporating geological dip and strike information, introduced recently by Scholl *et al.* (2015).

## INVERSION MODELLING METHODOLOGY

The core of the inversion modeling code, implemented for Marine, Land and Airborne streamer and nodal EM, is a 2.5/3D forward algorithm based on a finite difference (FD) frequency domain formulation. The related equations are solved with iterative solvers, accelerated using a multigrid preconditioner (Mulder, 2006). For time domain EM, responses are computed either by transforming the frequency domain responses to time domain (2.5D), or an implicit time stepping process (3D).

The FD grids are set up individually for each measurement point, independently from the model discretization (Druskin and Knizhnerman, 1994). The FD and model grids are generated on the fly based on the specific EM system configuration, model resistivities and frequencies/decay times, following rules similar to those presented in Hördt (1992) and Plessix *et al.* (2007). The model is sampled onto the FD grid cells using material averaging (e.g. in Commer and Newman, 2008). In order to more accurately represent rugged topography (or bathymetry in the marine EM case) the model grid may be unstructured in the vertical direction (Scholl and Sinkevich, 2012).

The example airborne frequency domain EM model grids in Figure 1 show the vertically unstructured model (above), and the related FD grids (below) for two positions of system.

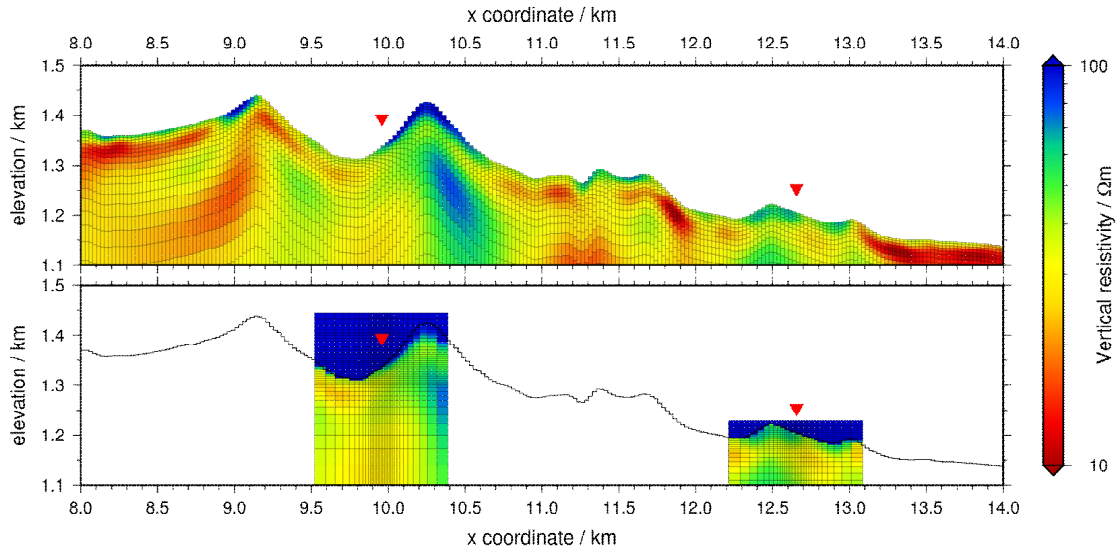


**Figure 1: Multi-grid AEM example, where the red triangles indicate two measurement points of a frequency domain (coincident) transmitter-receiver system. Top: the model cells follow the topography in this example, but also may be set up strictly horizontal, based on a priori knowledge of the stratigraphy. Bottom: FD grid cells for two positions. (Note that the air cells are not shown.)**

The inversion acts on the model grid (Scholl *et al.*, 2004). When set up to use only a smoothness operator, the inversion minimizes the cost function

$$\Phi(\mathbf{m}) = \|(\mathbf{d} - \mathbf{f}(\mathbf{m}))\|^2 + \beta \int_V \|\nabla \mathbf{m}\|^2 dV$$

The first part is the misfit between the data vector  $\mathbf{d}$  and the synthetic data  $\mathbf{f}(\mathbf{m})$  for model vector  $\mathbf{m}$  (dropping a weighting matrix for brevity). The second term defines some smoothness operator with  $\nabla \mathbf{m}$  signifying the model gradient. The trade-off parameter  $\beta$  on the smoothness terms is lowered over the course of the inversion to ultimately fit the data on average within their error estimate. The cost function is minimized using a Gauss-Newton (2D, see Constable *et al.*, 1987) or a Quasi-Newton (3D, Plessix and Mulder, 2008) approach.

### CROSS-GRADIENT REGULARIZATION

Gallardo and Meju (2003) introduced the cross-gradient concept for the joint inversion of different geophysical methods; 2D DC resistivity and seismic in that specific case. The idea is to quantify structural similarity between two property distributions, rather than inter-property correlation, by looking at the norm of the cross-product of their gradients. This norm is zero if the directions of change in the two models are aligned. It is irrelevant if model values increase or decrease in that direction. Likewise, the strength of the change does not matter.

We add the cross-gradient term as an additional regularization term to the inversion cost function:

$$\Phi(\mathbf{m}) = \|(\mathbf{d} - \mathbf{f}(\mathbf{m}))\|^2 + \beta \int_V \|\nabla \mathbf{m}\|^2 dV + \gamma \int_V \|\nabla \mathbf{m}_A \times \nabla \mathbf{m}_B\|^2 dV$$

The vectors  $\mathbf{m}_A$  and  $\mathbf{m}_B$  contain two different properties sampled on the same model grid. For a simultaneous joint inversion as shown in Figure 2,  $\mathbf{m}_A$  and  $\mathbf{m}_B$  are both part of the total model vector  $\mathbf{m}$ ; i.e.  $\mathbf{m}_A$  contains all resistivities while  $\mathbf{m}_B$  contains the densities, and  $\mathbf{m}$  contains both. For the subsequent geosteered inversion examples, however,  $\mathbf{m}_B$  contains some nominal values that define a geological a priori structure. In this case, the total model vector  $\mathbf{m}$  contains only  $\mathbf{m}_A$ , and  $\mathbf{m}_B$  is not altered during the inversion. Instead of  $\mathbf{m}_B$ , it is possible to directly provide gradients  $\nabla \mathbf{m}_B$ , as shown in Example 1 below.

The additional regularization term comes with its own trade-off parameter  $\gamma$ . We found it useful to keep  $\gamma$  constant, while lowering  $\beta$  in order to reach the desired misfit. Using the cross-gradient part as sole regularization did not stabilize the inverse process adequately, so additional regularization, e.g. in form of the smoothness term, was necessary.

The equation above assumes that all model vectors contain dimensionless quantities. The overall magnitude of  $\mathbf{m}_A$  or  $\mathbf{m}_B$  is not relevant for the cross-gradient regularization, as it will only affect the strength of the regularization, which is something that has to be adjusted with trade-off parameter  $\gamma$  anyways. It is possible, however, to scale e.g. the a priori gradients based on how reliable the a priori information is in a certain part of the model relative to other parts. For example, in the case illustrated below where surface

dips are used to regularize the inversion, the dip-derived gradients are scaled down with depth to reflect that the dips are well known at the surface but become increasingly uncertain at depth.

3D AEM and AGG inversions were carried out on a synthetic model of  $4,512 \times 4,512 \times 1,000$  m, discretised in  $40 \times 40 \times 17$  cells, containing three separate anomalous bodies within 150 m from surface (Figure 2). AGG data were generated for 3721 measurement points for the gravity component  $g_z$  and the gravity gradient components  $g_{xx}$ ,  $g_{xy}$ ,  $g_{yy}$  and  $g_{zz}$  for a total of 18,605 data points. Noise was added, with standard deviations of  $2\% + 0.2$  mGal, and  $2\% + 5$  Eötvös, respectively. Frequency domain AEM data were generated for 196 measurement points, using 3 frequencies, a coplanar coil configuration, and adding 2% noise.

Model slices at 60 m depth and cross-sections at 2.13 km north illustrate the results. While the single inversions (sub-figures b and e) reproduce the original model reasonably well, the bodies in the AEM-alone inversion are too thin, and are not well separated laterally. The AGG-alone in particular lacks definition at the top of the red anomaly.

The joint inversion results in subfigures c) and f) show clearly separated anomalies in the AEM result, and better vertical definition for both properties. Moreover, the structures are far more similar than in the single inversion results in that outlines of bodies for the two resulting models match much better.

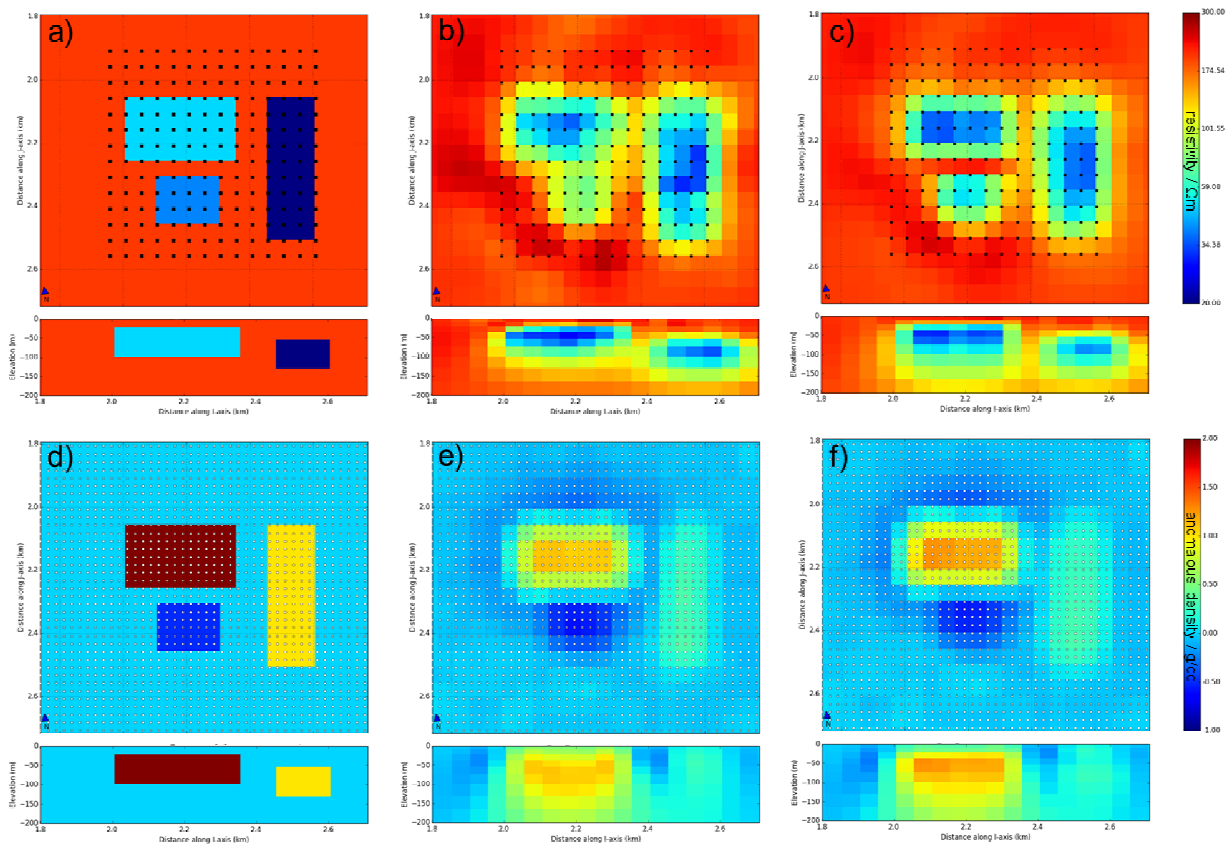


**Figure 2:** Example simultaneous joint inversion of AEM and AGG data; the upper and lower rows show resistivity and density models, respectively. AEM sites = black squares, AGG sites = white circles. The left hand panels a) and d) are the input models, the central panels b) and e) are the single domain inversions, and the right hand panels c) and f) are the simultaneous joint inversion using the cross-gradient regularization. (Area shown is  $0.9 \times 0.9$  km, and section is 0 to 200 m.)

### GEOSTEERED INVERSION

Instead of only comparing the model gradients of two different property volumes inverted simultaneously, it is possible to introduce a priori gradients derived from an auxiliary model or data set. In this case  $\mathbf{m}_A$  is identical to the inverted model vector  $\mathbf{m}$ , while  $\mathbf{m}_B$  is the auxiliary a priori model that remains unaltered during the inversion. Since only the direction of change matters, arbitrary numerical values can be used to create an auxiliary model resembling geological structures. Alternatively, gradients might be defined directly without setting up a model containing nominal values, so instead of creating some auxiliary model  $\mathbf{m}_B$ , the gradients  $\nabla \mathbf{m}_B$  are used as inversion input.

**Example 1: Using surface geological dips from Alberta foothills**

Time domain AEM data (CGG HELITEM) were surveyed in the Alberta foothills area, as part of a 2014 near-surface characterization program. The stand-alone (i.e. without cross-gradient) smooth model 2D inversion shown in Figure 4e captures the main geological units, but the shape of the anomalies fade out quickly and dips are not very obvious.

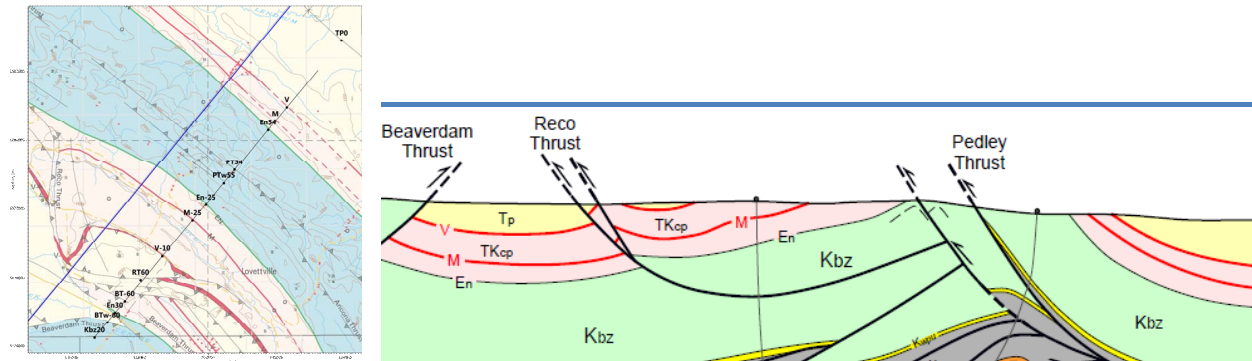


**Figure 3: Segments of geology map and cross-section (blue trace) from Langenberg and LeDrew (2001), with AEM line overlain (black trace) and annotated with dip values projected to line from the ground data published on the geology map.**

Ground measurements of dip and strike are available from the published 1:50,000 geology map (Langenberg and LeDrew, 2001) along with interpreted cross-sections, through areas adjacent to the AEM area, that illustrate the compressive structural style; outcropping steep thrusts cutting the related fold structures (the relevant part of the closest cross-section is shown in Figure 3).

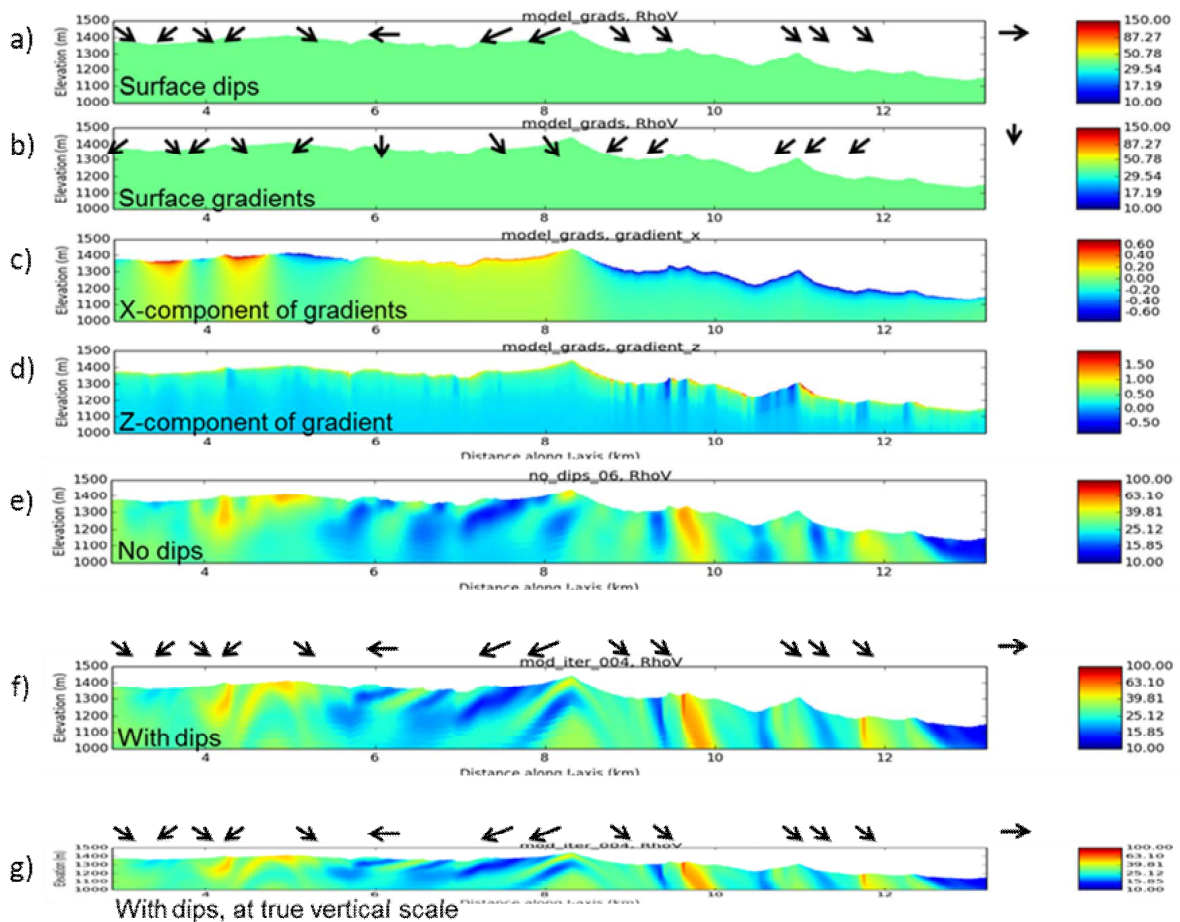


**Figure 4: 2D AEM cross-gradient inversion with surface dips (located Figure 3). Arrows in panels a) and e)-f) roughly indicate the direction of the surface dip and the position of the related contacts; arrows in b) show the derived gradients, perpendicular to the dips; further from top to bottom: the x- and z- component of the surface dips (c and d), interpolated between points and smoothed downwards; Standard (“No dips”) 2D smooth model AEM inversion (e); 2D AEM inversion using dips, plotted with  $\times 2$  (f) and  $\times 1$  (g) vertical exaggeration. Pedley Thrust is at 9.5 km.**

The scattered dip measurements were projected onto the AEM line following the mapped geological contacts (Figure 3 and Figure 4a). The surface dips were then converted to gradients (simple 90° relationship, Figure 4b) interpolated between the projected dip measurement points. While the dips are well defined at surface, they will change with depth, so in order to fade out the cross-gradient regularization accordingly, the gradients are increasingly smoothed downwards (Figure 4c, d). When compared to the blind inversion results (Figure 4e) both close to the surface and below, the geosteered inversion provides a more realistic structural model (Figure 4f, g). In similar workflows the code facilitates surface geology constraint of a range of single or multiple geophysical domain inversions, including for instance potential fields and seismic.

**Example 2: AEM over Maimon sulfide deposit, with auxiliary model from regional geological dip and strike**

Frequency domain EM data were collected in 2007 above a known volcanogenic massive sulfide deposit in a rugged sector of the Cordillera Central of San Domingo, covered a sequence of Cretaceous metavolcanics (Roos *et al.*, 2007). The data were recorded with a DIGHEMV system (Fraser, 1972) in a frequency range of 915 Hz to 56 kHz with two coaxial and three coplanar coil pairs. The nominal flight height was 40 m above ground level, and the altimeter data from the survey were used as topography in the 3D model. Figure 5 (left) shows the position of the flight lines and the trace of the deposit and the data for the lowest frequency. For the south-easternmost line, the position of the deposit is associated with peak EM response. For the adjacent flight lines, however, the peaks are shifted to the south-west.

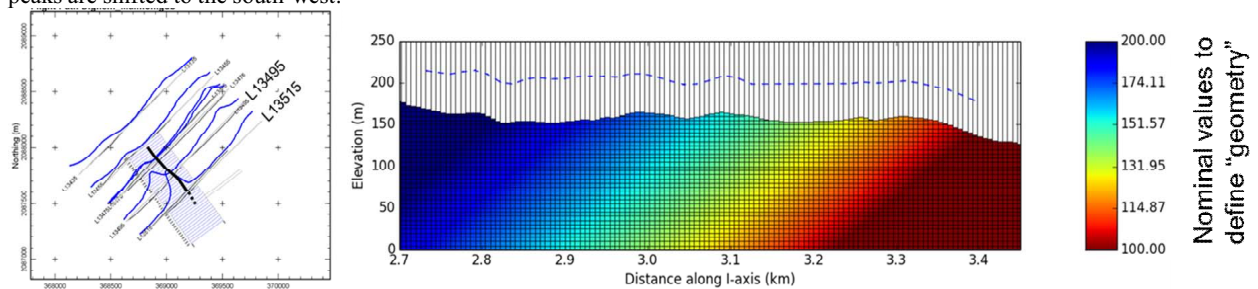


**Figure 5: Flight lines and data for the lowest frequency; the black line marks the position of the orebody (from Smith and Hodges, 2008) (left); in-line section through the auxiliary model used to define the 45 degree dip (right).**

Following the regional dips given in Roos *et al.* (2007) a model of arbitrary values was set up that exhibits dips of 45 degrees (Figure 5). The 3D inversion was set up to produce a smooth model with structures predominantly parallel or antiparallel to the steering model. The result of a standard smooth model inversion and an inversion incorporating the dip information is shown in Figure 6.

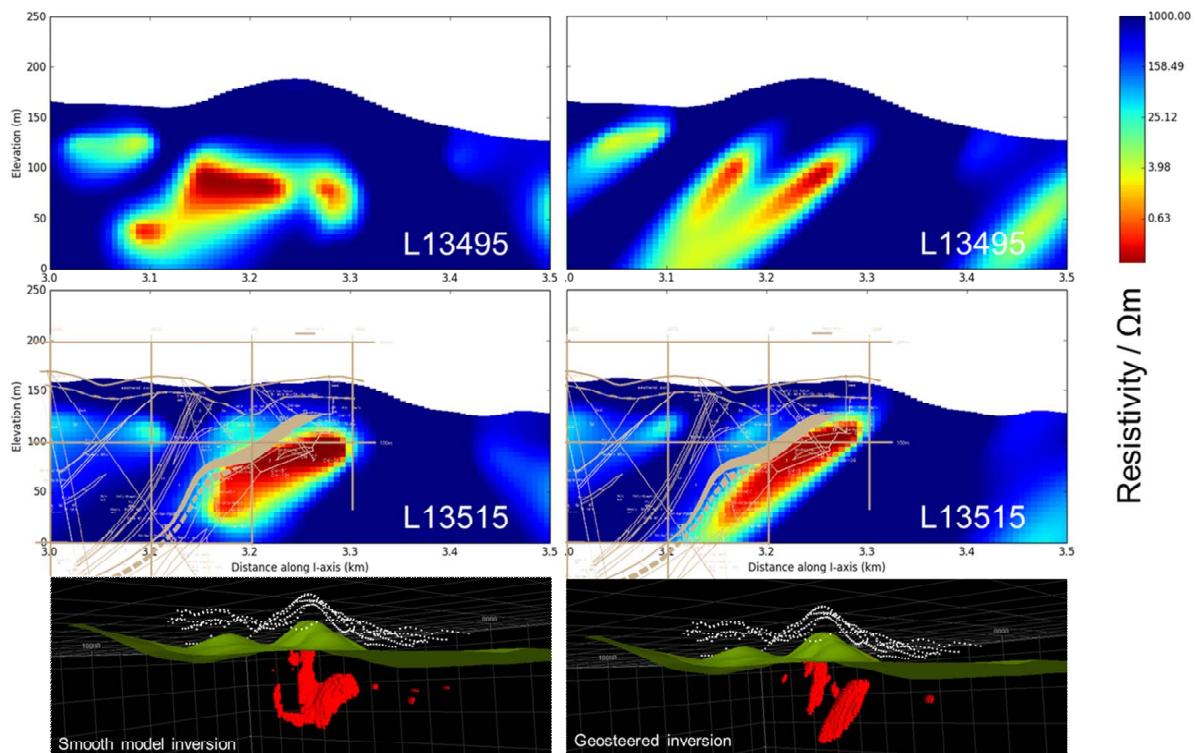


**Figure 6: 3D inversion results with standard smoothing (left column) and with cross-gradients (right column); the top and center rows show sections through the model at flight lines L13495 and L13515, respectively. Superimposed on the plot for line L13515 is a geological cross section obtained from drilling (after Smith and Hodges, 2008); lowermost row shows the conductive body as isosurfaces at <1 Ωm. White dots indicate the flight path.**

Roos *et al.* (2007) give a section of the ore body along line L13515 derived from drilling a sketch of which is superimposed on the centre row of Figure 6. The results for the smooth model inversion seem reasonable at first glance, but the geosteered result better matches the given geology. There are differences also in how the body changes in the cross-line direction, due to the laterally shifted EM response peaks. The smooth model inversion produces a semi-continuous body that wraps around and neither matches the regional dip, nor the position of the known orebody (black trace in Figure 5 left). The geosteered inversion result keeps the main conductive sheet within the defined dip and strike, fading it out slowly along strike towards the north-west, and models the shifted peak in data by a separate, sub-parallel sheet.

## CONCLUSIONS

We have implemented the quantitative use of surface or sub-surface geological data during 2D and 3D inversion modeling, providing a result that is consistent with all available data, and hence of increasing plausibility. This is accomplished through steering the inversion using cross-gradient regularization, where the reference gradient model is derived directly from geology. The methodology is generic, and therefore expandable to derive a controlling gradient field from the range of sub-surface attribute data available in exploration and development projects.

## ACKNOWLEDGMENTS

Geological sections for the massive sulfide case are shown by courtesy of Globestar Mining Corporation. We thank CGG for providing the AEM data sets, and facilitating the publication of this work.

## REFERENCES

- Constable, S. C., Parker, R. L. and Constable, C. G., 1987, Occam's inversion: A practical algorithm for generating smooth models from electromagnetic sounding data. *Geophysics*, **52**, 289-300.
- Commer, M. and Newman, G.A., 2008, New advances in three-dimensional controlled-source electromagnetic inversion. *Geophys. J. Int.*, **172**, 513-535.
- Cox, L.H., Wilson, G.A., and Zhdanov, M.S., 2012, 3D inversion of airborne electromagnetic data. *Geophysics*, **77**, No. 4, WB59-WB69.
- Druskin, V. and Knizhnerman, L., 1994, Spectral approach to solving three-dimensional Maxwell's diffusion equations in the time and frequency domain. *Radio Science*, **29**, 937-953.
- Gallardo, L. A. and Meju, M. A., 2003, Characterization of heterogeneous near-surface materials by joint 2D inversion of dc resistivity and seismic data. *Geophys. Res. Lett.*, **30**, 1658.
- Fraser, D.C., 1972, A new multicoil aerial electromagnetic prospecting system. *Geophysics*, **37**, 518-537.
- Hördt, A., 1992, Interpretation transient elektromagnetischer Tiefensondierungen für anisotropy horizontal geschichtete und für dreidimensionale Leitfähigkeitstrukturen. Mitteilungen aus dem Institut für Geophysik und Meteorologie der Universität zu Köln, **86**.
- Langenberg, C.W., and LeDrew, J., 2001, Geological Map: Coal Valley, NTS Mapsheet 83F/2, 1:50,000 map with cross sections. Alberta Geological Survey Map 237.
- Mulder, W. A., 2006, A multigrid solver for 3D electromagnetic diffusion, *Geophys. Prosp.*, **54**, 633-649.
- Plessix, R.-E. and Mulder, W. A., 2008, Resistivity imaging with controlled-source electromagnetic data: depth and data weighting. *Inverse Problems*, **24**, doi:10.1088/0266-5611/24/3/034012.
- Roos, P., Burgess, H., and Ward, I., 2007, Updated Mineral Resource And Reserve Estimate, Cerro De Maimón Project, Msnr. Nouel Province, Dominican Republic. Technical Report NI 43-101 for GlobeStar Mining Corporation.
- Scholl, C., R. Martin, O. Koch, S. L. Helwig, B. Tezkan, DESERT research group, 2004, 2.5-D inversion of transient electromagnetic data. Abstracts of the 17th International Workshop on Electromagnetic Induction in the Earth, Hyderabad, India.
- Scholl, C., Neumann, J., and Watts, M.D., 2015, Geosteered 3D Inversion of AEM Data in Rugged Terrain, 1st European Airborne EM Workshop, Turin, Italy.
- Scholl, C. and Sinkevich, V. A., 2012, Modeling mCSEM data with a finite difference approach and an unstructured model grid in the presence of bathymetry. Abstracts of the 21st EM Induction Workshop, Darwin, Australia.
- Smith, R., and Hodges, G. 2008, The HeliGEOTEM system, with an example of data from the Maimon deposit in the Dominican Republic. Proceedings of AEM2008 – 5th International Conference on Airborne Electromagnetic, Finland 28–30 May 2008.
- Vallée, M., and R. Smith, 2007, Comparison of fixed-wing airborne electromagnetic 1D inversion methods. Proceedings of Exploration 07: 5th Decennial International Conference on Mineral Exploration, 1067–1072.